ANNALS OF GEOPHYSICS, 69, 1, NS102, 2026; doi:10.4401/ag-9278
OPEN ACCESS

Research on Conventional ERT Inversion and Improved AMT Inversion Based on Deep Learning Denoising Data in Tunnel and Road Detection: A Case Study in Sichuan Province

Jue Wang[1], Shuang Liang[*,2], Kai Zeng[3], Xing Lan[4]

(1) Chengdu Vocational and Technical College of Industry, Architectural Engineering Institute, Chengdu, China
(2) City University of Hefei, Civil Engineering Department, Hefei, China
(3) Public Welfare Second-class Institution, The 6th Geological Brigade of Sichuan, Luzhou, China
(4) Sichuan Metallurgical Geological Survey and Design Group Co,Ltd., Chengdu, China

Article history: received January 29, 2025; accepted January 8, 2026

Abstract

The safety of tunnels and roads is crucial for traffic safety. Due to the presence of adverse geological features, which can cause serious problems in tunnels and on roads, there is an urgent need for comprehensive geophysical investigations to determine their distribution. This will provide additional technical information to help ensure the safety of engineering projects. This study uses the tunnels and roads in Jiulong County, Sichuan Province, as an example. Integrated geophysical methods were employed to arrange ERT sections at tunnel entrances and exits, as well as on geophysical slopes. The primary focus was on the thickness of the overlying layers and the geological conditions of the rock and soil within a certain depth range above the tunnel design line. For the longitudinal cross-section of the main tunnel, Audio Magnetotelluric (AMT) were primarily used to investigate fault zones, karst formations, aquifers and rock mass grades. Combining electromagnetic data denoising and inversion using a U-Net neural network with ERT inversion clearly revealed the underground geological conditions of the tunnel. The tunnel alignment is characterised by a mixture of stable quartz-rich rock masses and metamorphic rock masses. Overall, the deep rock mass of the tunnel axis is stable, with fractures in some transverse sections. The intersection is relatively stable, interspersed with weathered and fractured zones. These findings provide valuable insights into advancing geophysical techniques for investigating tunnel sites under complex geological conditions.

Keywords: Geophysical exploration; Deep learning; Audio magnetotelluric; Electrical resistivity tomography; Fracture zones

1. Introduction

The safety of tunnels and roads is very important for people's traffic safety (Pietro, 2023). In recent years, as the existence of undesirable geological bodies in tunnels and roads will cause serious problems, there is a need to explore

the distribution of undesirable geological bodies in tunnels and roads, to provide more technical information in order to ensure the safety of traffic. At present, there are quite a few near-surface geophysical methods that are often used to explore the underground situation(Guo, 2020). For example, ground penetrating radar (GPR) (Russolillo et al., 2024; Wang et al., 2015; De Benedetto et al., 2012), electromagnetic (MT) (Rathnayaka et al., 2024; Wang et al., 2022; Ghalati, 2022; Gomo, 2023; Modreck, 2023;Wang et al., 2018; Deshmukh et al., 2022; Ren et al., 2023; Wang et al., 2017; Kiyoshi et al., 1999; Wang, 2017), electrical resistivity tomography (ERT) (Wang et al., 2022; Moreira et al., 2021; Verdet et al., 2020; Fäth and Kneisel, 2024; Park et al., 2022; Imani et al., 2021; Russolillo et al., 2024; Genetu and Mewa, 2023; Wang et al., 2015; Zhu, 2017). Of all the geophysical methods mentioned above, they have their advantages and disadvantages under different exploration conditions. However, they are all characterised by non-destructive exploration without damaging tunnels and roads. Therefore, most geophysical methods can be used to characterise these undesirable geological bodies and analyse their distribution in the subsurface. Additionally, Araya-Polo et al. (2018) proposed a deep-learning-based tomography method that leverages neural networks to automatically extract hierarchical features (Furthermore, LeCun et al., 2015), directly generating velocity models from raw seismic data, significantly enhancing the efficiency and automation of geological detection in tunnels and roads. The study reveals the results of a combined application of audio magnetotellurics (AMT) and electrical resistivity tomography (ERT) of geophysical exploration to identify undesirable geological bodies hidden in the subsurface.

ERT is one of the geophysical methods to determine the subsurface resistivity distribution by measuring the potential difference directly on the road near-surface or tunnel near-surface. Currently, it is successfully applied in many scenarios. Moreira et al. (2021) reveal the relationship between fluid dynamics and soil structure using ERT. Verdet et al. (2020) undercover karst features are found with 3D ERT geostatistical model. Fäth and Kneisel (2024) study the temporal resistivity changes in woodland soils with the help of ERT. Combined with the regularity of resistivity distribution, Russolillo et al. (2024) find similarities of buried fortification anomalies. ERT is also effective in landslide investigation(Imani et al., 2021; Genetu and Mewa, 2023). At the same time, the method has been used with successful results in exploration of tunnels and roads. Doğukan (2023) make use of a combination of geophysical ERT and MASW for buried tunnels near the surface. Especially, when determining resistivity anomalies that are blurred at the deep location, many researchers have tried to solve this problem by applying other geophysical methods. For instance, Fichtner et al. (2019) proposed the Hamiltonian Monte Carlo (HMC) method, which integrates Hamiltonian dynamics with adjoint techniques to efficiently address high-dimensional linear and nonlinear geophysical tomography inverse problems.

AMT is one of the geophysical methods for exploring subsurface resistivity anomalies at greater depths of exploration and with ease of operation. By taking advantage of the large depth of propagation of electric and magnetic fields, deeper resistivity distribution features can be obtained. Many academias have studied this method. For example, groundwater investigations (Rathnayaka et al., 2024), karst investigations (Ende, 2012), quaternary deposits investigations(Wang et al., 2022). Most of scholars image undesirable geological bodies in tunnels and roads by AMT. Zhao et al. (2021) directly and accurately analyse the location and size of the distribution of hidden extraction zone in the tunnel through magnetotellurics imaging results. He et al. (2006) successfully apply electromagnetic (EM) methods and controlled source audio magnetotellurics (CSAMT) to the mountain tunnel route. However, the field data acquisition process receives a variety of environmental noise, and many researchers have tried different methods to reduce the influence of noise on the final results.

In the past few decades, many traditional methods have emerged for suppressing MT noise. Among them, classic denoising methods include wavelet transform (Garcia et al., 2008), singular value decomposition (SVD) (Li et al., 2021; Li et al., 2022), sparse representation (Li et al., 2024; Zhang et al., 2022), empirical mode decomposition (EMD) (Cai et al., 2015; Guo et al., 2022), and mathematical morphological filtering (Li et al., 2020). However, these traditional strategies have their inherent drawbacks. For example, wavelet transform methods face challenges in selecting appropriate wavelet basis functions to handle complex noise and signal components (Trad et al., 2000). The SVD method assumes a linear combination of signal and noise, which limits its application effectiveness in scenarios characterized by nonlinear noise (Aharon et al., 2006). Sparse representation methods require careful selection of appropriate dictionaries, as different choices may lead to variations in denoising results (Tang et al., 2018). The EMD method is prone to mode mixing between the intrinsic mode functions (IMFs) of the signal. When the intrinsic frequencies of two or more IMFs are similar or overlap, it can lead to imprecise decomposition (Wu et al., 2009). These limitations limit the widespread application of traditional methods in MT denoising scenarios.

In order to address the above challenges, research on MT noise suppression using deep learning (DL) has made rapid progress. These methods have demonstrated their excellent predictive performance and generalization

ability in DL (Neyshabur et al., 2017; LeCun et al., 2015; Li et al., 2022; Fang et al., 2023), effectively surpassing the limitations of traditional methods (Li et al., 2022; Li et al., 2020). For example, Aleardi et al. (2022) employed a residual neural network (ResNet) to accelerate probabilistic electrical resistivity tomography (ERT) inversion, replacing the computationally intensive finite element forward operator by learning the nonlinear mapping between model parameters and apparent resistivity data, thereby substantially reducing computation time while preserving inversion accuracy. Especially in the field of transfer learning, DL has the potential to utilize pre-trained models in different MT environments, significantly improving its applicability on different noisy data.

In recent years, the latest progress in MT research has mainly focused on exploring various DL network models, such as convolutional neural networks (CNNs) (Shea et al., 2015) and recurrent neural networks (RNNs) (Medsker et al., 2001; Chen et al., 2020), to achieve denoising of MT data. Therefore, in order to improve the inversion accuracy, this article uses AMT data based on deep learning denoising for its inversion.

2. Background overview

2.1 Natural geographical overview

The work area is located in Sichuan Province, and belongs to the section of the Shimian to Derong Highway. The route goes with a tunnel through MuerGua-mountain and a total length of about 81.1 km, shown in Fig. 1.

The project route is roughly spread along Mawo Ditch and Regu Ditch, both of which have perennial water flow, and the overall surface water system development in the survey area. Some of the working points of the tunnel are located in high altitude areas, and it is necessary to find water sources by themselves when investigating.

A total of 7 ERT sections with a total length of 4.23 km and 7 AMT sections with a total length of 13.68 km were completed in this geophysical survey. Only a few mountain roads can be passed along the working section, and

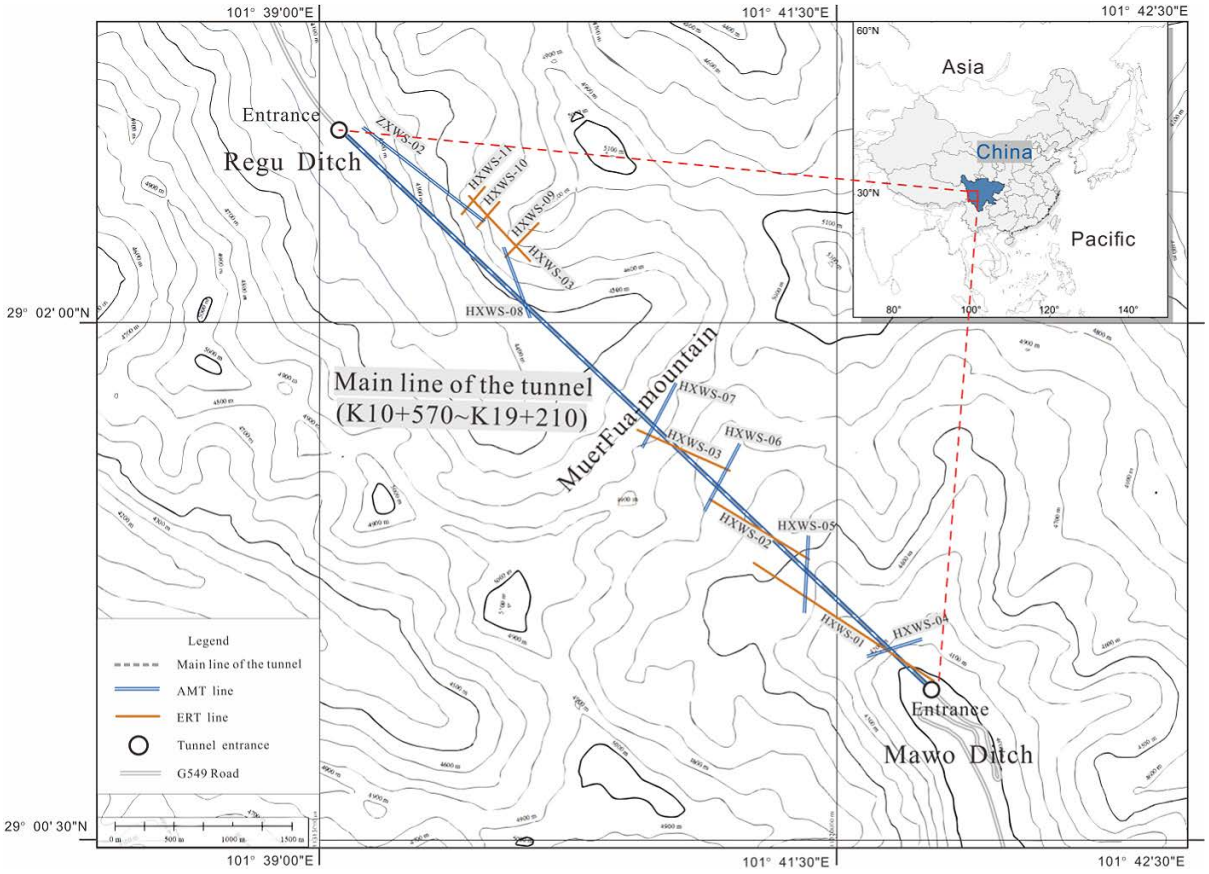

Figure 1. Spatial arrangement of tunnels and geophysical profiles.

the design alignment of most sections is far away from the existing highway, with large height difference, no road communication and lush vegetation, and the traffic conditions are poor.

The project is located at the edge of the western Sichuan Plateau, with rugged terrain, continuous mountains, alternating peaks and valleys. The terrain is high in the middle of the route and low at both ends. The highest point is in the middle of MuerGua-mountain Tunnel, with an altitude of 4,900 m.

The fluctuation of the route section is huge, mainly manifested in mountainous landform. The climate change in the working area is great, and it often snows, which has a great impact on this work.

2.2 Geographical overview

The stratigraphic framework of the survey area is characterized by extensive Quaternary overburden unconformably overlying a crystalline basement (Hu et al., 2024). The Quaternary deposits are genetically diverse, primarily consisting of Upper Pleistocene glaciofluvial outwash, Holocene alluvial-proluvial sediments, aeolian deposits, and eluvial-deluvial slope deposits, as well as accumulations from geological hazards such as landslides and debris flows (Tie et al., 2024). The underlying bedrock is dominated by intrusive magmatic rocks, including biotite granodiorite and quartz diorite, interlayered with high-grade metamorphic sequences such as biotite felsic gneiss and other gneissic complexes (Yang et al., 2024).

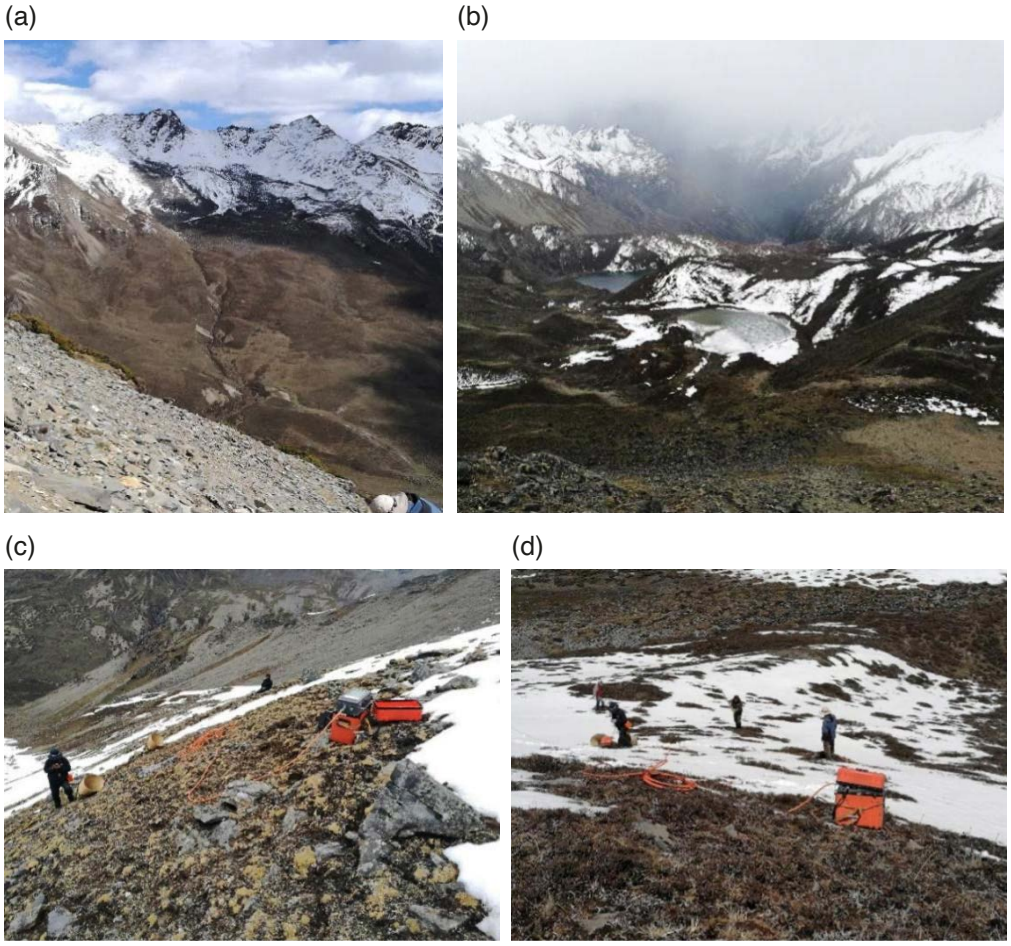

Figure 2. The typical geomorphology and field data acquisition environment in the study area. (a,b) The region is characterized by high-relief mountainous terrain with steep slopes and deep valleys. The surface geology is dominated by Quaternary Holocene deposits – including alluvial, proluvial, slope wash, and colluvial materials – and Upper Pleistocene glaciofluvial deposits, which overlie a bedrock of biotite granodiorite and gneiss. (c, d) Field crews conducting geophysical surveys under challenging climatic conditions. These panels show the deployment of the EM3D electromagnetic exploration system on steep, vegetated slopes (c) and snow-covered ground (d).

There are many kinds of aquifers in the working area, such as loose rock pore aquifer, structural fracture aquifer and weathered zone fracture aquifer. The structural fracture aquifer has the greatest influence on the construction of highway tunnel engineering, and occupies a prominent position in the engineering geological conditions of highway construction, and is the main type of groundwater in the structural fracture aquifer area.

The phenomenon of rock weathering is very common in the region, so that there are widely fractured aquifers of weathering zone network in all kinds of strong weathering zones of rock mass. The groundwater in the fractured aquifers of weathering zone network is mainly replenished by atmospheric precipitation and affected by the topography and geological structure conditions of mountains and valleys, and most of them are characterized by near-path recharge and nearby drainage. Although the amount of groundwater in such groundwater aquifers is limited, its impact on roadbed slopes is very common.

According to the occurrence, burial conditions and hydrodynamic characteristics of groundwater along the route, groundwater can be divided into two categories: loose rock pore water and bedrock fissure water.

2.2.1 Loose rock pore water

It mainly occurs in the quaternary and quaternary loose deposits, distributed in the gully beds along the line and the areas with slow terrain. The loose materials are mostly composed of alluvial diluvium, landslide deposit, moraine sand, gravel, crushed stone soil and sub-sandy soil, which receive atmospheric precipitation, snow and ice meltwater or surface water. It is mainly distributed in river valleys. According to relevant data, it is revealed that the aquifer thickness is 42.90 ~ 60.15 m, and the aquifer is composed of the upper Holocene drift stone and the lower Upper Pleistocene alluvial sand and fine sand. The groundwater level buried depth is 0.35 ~ 2.50 m, and the permeability coefficient is 45.66 m/d ~ 60.83 m/d. The chemical type of groundwater is mainly calcium carbonate type. The salinity is generally 0.1-0.15 mg/l, and the PH value is about 7.0-7.5. The diving depth and runoff conditions vary from place to place, and the drainage conditions and water level are greatly affected by atmospheric precipitation. When the water level rises sharply during heavy rainfall, the high dynamic water pressure is generated due to poor drainage, which reduces the shear strength of soil and leads to slope instability and collapse.

2.2.2 Bedrock fissure water

The water in bedrock fissure is distributed in the vast mountains of bedrock and is mainly controlled by structure and weathering. Bedrock fissure water, especially in a certain depth range of rock and soil surface, can produce dynamic water pressure, and in cold and frozen climate, it can be iced, thus aggravating the development and penetration of cracks, and often lead to slope bedrock collapse. Bedrock fissure water includes two types: structural fissure water and weathering fissure water.

Structural fissure water mainly exists in the back, synclinal core zone and fracture zone, and the crushed rock mass in the fracture affected zone, mainly receives the infiltration and recharge of atmospheric precipitation and ice and snow meltwater, and drains to low-lying places or in the form of springs along the characteristics of the accumulation and migration of structural plane cracks. The groundwater dynamic changes obviously with the season and is closely related to the development degree of structural cracks. The overall water richness is medium to poor. The spring flow is generally 0.1-1.0 L/s. The water-bearing rock group consists of biotite granodiorite, quartz diorite and biotite felsic gneiss. The rock is hard and dense, and the fractures are relatively developed under the influence of multi-stage tectonic movement, mostly conjugate shear fractures. According to the early field survey, the surface of the crack has a large opening degree after weathering, generally 1-3 mm wide, some up to 5-10 mm, and its continuity is good.

Weathering fissure water mainly occurs in the network weathering crevices of bedrock, and is mainly recharged by atmospheric precipitation and meltwater of ice and snow. It slowly migrates and drains along the crevices towards low-lying areas. The groundwater dynamics change obviously with the season, which is closely related to the development degree of cracks and the properties of fissure fillings, and the distribution and water abundance are extremely uneven. The weathering crust is mostly within 20 m thick. The spring flow is generally 0.13-1.5 l/s. In the route survey area, the development degree of bedrock differentiation fissure is different, so the overall water richness is moderate to poor.

2.2.3 Groundwater recharge, runoff, and discharge conditions

The groundwater recharge is mainly precipitation, ice and snow melt water and frozen layer melt water, and also includes valley surface water in the quaternary loose accumulation area in the low-lying area of river valley. In this area, the quaternary loose deposits develop, and due to the internal and external dynamic geological processes, especially the cold physical weathering, the surface bedrock rocks are broken and cracks develop, and the infiltration of atmospheric precipitation, ice and snow meltwater, frozen layer meltwater, and river and lake water forms Quaternary pore water and bedrock fracture water. After receiving recharge, under the action of gravity, Quaternary pore water and bedrock fracture water are formed. Groundwater runoff is formed along the pores of quaternary loose deposits and rock fissures, in which a part of bedrock fissures water is directly injected into the gully, and a part of bedrock fissures recharge the quaternary loose deposits to form quaternary pore water. In addition, during the migration of fissure water, due to the change of topography and lithology in local areas, the groundwater is exposed to the surface through erosion, cutting or local obstruction, forming spring water and discharging to the surface to form surface water. Most of the quaternary pore water is directly injected into the gully and valley to form surface water, and a small part is discharged in the form of evaporation. The groundwater flow direction is consistent with the slope direction, and the hydraulic slope of the water surface is basically consistent with the slope of the surface topography.

3. Materials and Methods

3.1 Audio Magnetotelluric (AMT)

Magnetotelluric sounding (MT) including Audio Magnetotelluric (AMT), Broadband Magnetotelluric (BBMT) and Long-period Magnetotelluric (LMT), with the advantages of low resistance sensitivity and large depth of detection, have an increasingly wide range of applications in both shallow and deep exploration, and are one of the commonly used geophysical methods for investigating depths from the near surface down to the upper mantle.

Magnetotelluric sounding (MT) was proposed in the early 1950s by the former Soviet scientist A.N.Ikhonov (1950) and the French scientist Cagniard (1953), and has developed into one of the major geophysical methods.

The magnetotelluric method uses natural planar electromagnetic waves as the field source, with frequencies ranging from n*0.0001 to n*100 Hz, when the telluric electromagnetic field is incident into the ground, part of it is absorbed and attenuated by the medium, and part of it is reflected to the ground. The reflecting ground part contains electromagnetic field information reflecting the electrical characteristics of the underground medium. By observing mutually orthogonal components of natural electromagnetic fields on the ground or under the sea. The observed apparent resistivity (or phase) – frequency curve can be obtained. The resistivity distribution at different depths can be obtained from the apparent resistivity-frequency curve using an inversion method, and the subsurface structure can be investigated. The magnetotelluric method is not shielded by the high resistivity layer, the detection depth is large, the reflection of the low resistivity layer (body) is sensitive and ADAPTS to various geological environments, so it has been widely used in the field of crust and upper mantle structure, energy, resources and environment detection. The following formula represents the relationship between the ground electromagnetic component and the earth resistivity under the condition of uniform isotropic earth medium, which is the most basic formula for MT (Nabighian and Macnae, 1991):

$$\rho = \frac{1}{\omega\mu}|Z|^2 = 0.2T\left|\frac{E}{H}\right|^2 \tag{1}$$

Where ρ is the resistivity, $\omega = 2\pi/T$ is the angular frequency, μ is the permeability, Z is the wave impedance, E is the electric field (unit mV/km), H is the magnetic field (unit gamma).

Magnetotelluric sounding (MT) and Audio Magnetotelluric (AMT) share the same principles and operational methods, differing only in the frequency range used. MT employs observation frequencies ranging from n 0.0001 to n × 100 Hz, with detection depths of n × 100 to n × 10,000 meters, making it suitable for deep geological structure exploration. Audio Magnetotelluric (AMT) operates at observation frequencies ranging from n × 0.01 to n × 1000 Hz,

with a detection depth of n × 10 to n × 1000 m, offering higher resolution for shallow geological structure exploration. Therefore, to investigate the stability of the deep rock mass structure along the tunnel axis, identify fault zones, karst features, aquifers, and surrounding rock classifications, the AMT method will be employed for geological exploration along the main tunnel's longitudinal section.

The AMT work in this study utilized the EM3D electromagnetic exploration system jointly developed by EMI Company and Geometrics Company, completing a total of 7 audio-frequency electromagnetic sounding profiles with a total length of 13.68 km. Electrode layout technique: As shown in Fig. 3, multiple electrodes were used in this study, with each pair of electrodes forming an electric dipole. To facilitate comparison and monitoring of electric field signals, their length is equal to the point spacing. Electrode pairs aligned with the survey line direction are called X-dipoles, with two pairs; those perpendicular to the survey line direction are called Y-dipoles, with one pair. The direction of the Y-dipole is perpendicular to that of the X-dipole, with an error of ±0.5°; the length error of the electrodes is within 0.5 meters. The magnetic rods must be at least 5 meters away from the main unit. To eliminate human-induced interference, the two magnetic rods must be buried underground at least 20 centimeters deep, with their directions perpendicular to each other, and the error must be controlled within the ±2°, ensuring they are level. The main unit must be placed on a platform at least 20 meters away from the magnetic rods.

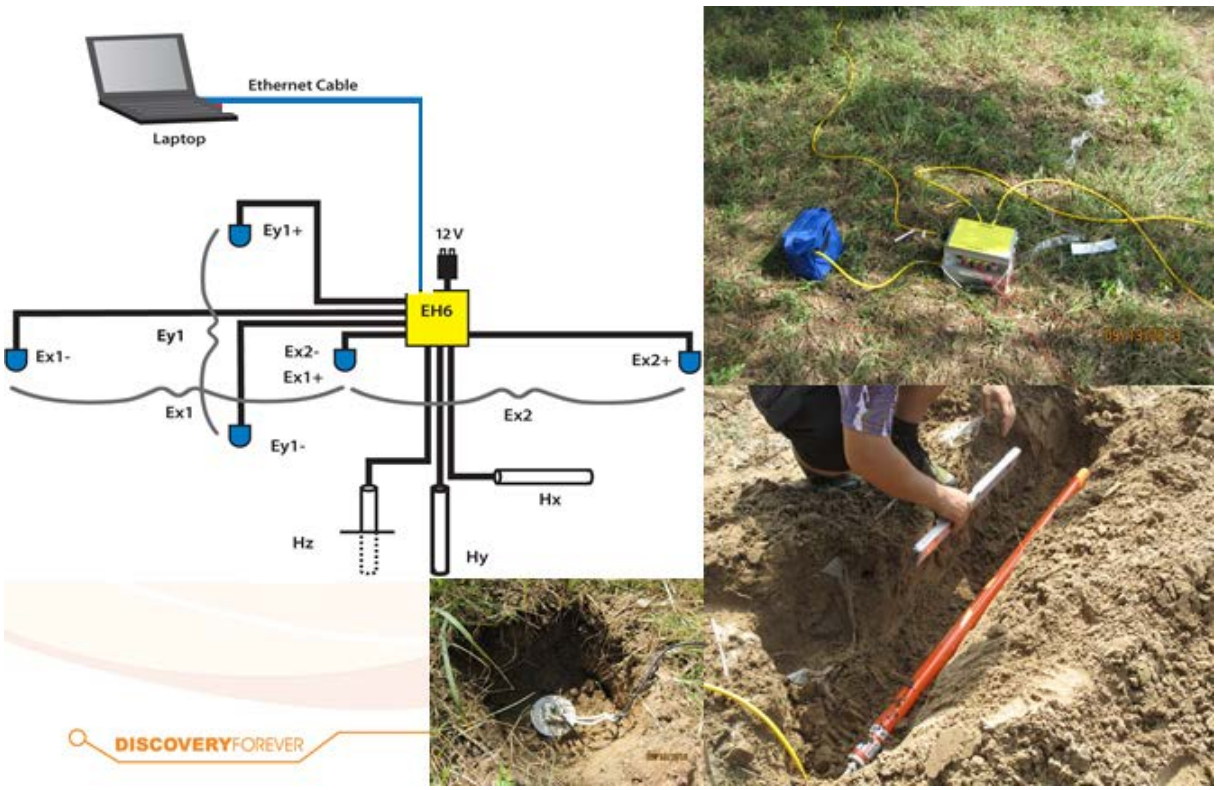

Figure 3. Schematic Diagram of Field Deployment for the EM3D Electromagnetic Survey System.

3.2 ERT

In direct current resistivity measurements, a generator is used to inject a current into the ground. The amount of current generated depends on the electrical conductivity of the subsurface medium. Charges accumulate at the interfaces between units of different electrical conductivities, thereby creating a potential difference. Data is obtained by measuring this potential difference between two surface or borehole electrodes. The measured voltage depends on the relative positions of the current electrodes and the target, as well as on the electrical conductivity of the subsurface layers. To obtain information on the spatial distribution of conductivity, multiple measurements must be taken at different locations and with different electrode configurations. Current I is supplied through electrodes A and B, and the potential difference ΔV between the measuring electrodes M and N

is measured (Fig. 4). The apparent resistivity value at the measurement point (between M and N) is then calculated using a general device coefficient formula:

$$\rho_s = K\frac{\Delta V}{I}$$
$$K = 2\pi\left(\frac{1}{AM} - \frac{1}{BM} - \frac{1}{AN} + \frac{1}{BN}\right) \quad (2)$$

Where ρ_s is the apparent resistivity, K is the device coefficient, ΔV is the Measured voltage, I is supplied current, AM, AN, BM and BN represent distance parameters respectively.

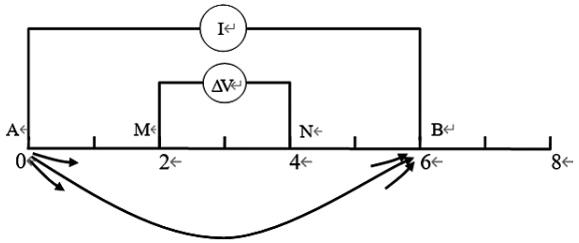

Figure 4. Working principle of ERT.

This ERT survey used the DZD-8 system produced by Zhongdi Zhuang (Chongqing) Geological Instruments. The system comprises a multifunctional direct current electrical resistivity meter and a multi-channel electrode converter.

For this project, the geophysical survey work involved arranging ERT sections at tunnel entrances and exits, as well as at survey slopes. This geophysical survey completed a total of 7 ERT profiles, with a total length of 4.23 km. The primary objective was to investigate the thickness of the overlying strata and the geological conditions of the rock and soil within a certain depth range along the planned route of the tunnel. Therefore, the Wenner array (α array) was selected for this survey. Advantages include stable measurement values and high resolution in detecting vertical variations in geological electrical properties. During measurement, AM = MN = NB represents one electrode spacing. The A, B, M and N electrodes were moved simultaneously to the right at each point to obtain the first profile line. Then, the spacing between AM, MN and NB increased by one electrode and the electrodes moved to the right at each point to obtain another profile line. This process was repeated to produce an inverted trapezoidal cross-section (Fig. 5). The device coefficient is k = 2πna, where a is the electrode spacing and n is the isolation factor. In this case, AM = BM = MN = na.

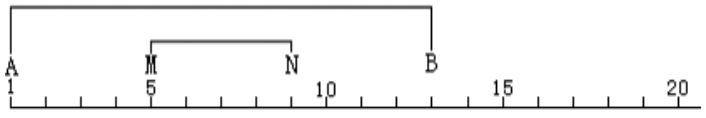

Figure 5. Wener device (α).

For this ERT exploration, 40-100 electrodes were used with a unit electrode spacing of 5 metres. The electrodes were laid out strictly according to the survey points. For this study, the work sites were mostly shrublands with favourable grounding conditions. To reduce the ground resistance of high-resistance electrodes, copper sulphate or saltwater was poured to keep the resistance of each electrode below 3 kΩ. Each electrode was buried to a depth of at least one-third of its height when laying them out to ensure uniform and close coupling with the ground. Full contact was maintained between the cable connections at each electrode interface and proper waterproofing and moisture-proof measures were implemented to ensure the quality of the collected data.

3.3 DL denoising

This section provides a detailed introduction to the conversion method of magnetotelluric signals into images and the composition of a denoiser based on depth Unet.

Firstly, converting one-dimensional magnetotelluric signals into two-dimensional images is considered as the process of denoising two-dimensional image data. The method of using deep learning based Unet neural network model for supervised learning has achieved good results, and compared with traditional model-based methods, it performs well in specific image denoising tasks. Therefore, we attempt to transform the denoising task of magnetotelluric signals into a discriminative denoising task based on image learning, so that the advantages of image denoising can help improve denoising performance. Due to the need for local sampling and connection perception in convolutional kernels, the conversion from signal to image is essential. Specifically, since each signal point has a crucial impact on the entire signal, it is necessary to transfer the signal points to the image mapping format of the image pixels, such as a grayscale image with one channel, where the image format is a natural transformation object. Therefore, for magnetotelluric signals, simply using the "reshaping" function as a widely used dimension change method in Python's Numpy library can convert one-dimensional signals into two-dimensional images, completing the conversion from direct signals to images. The transformation method is shown in Fig. 6.

The Fully Convolutional Networks(FCN) for image and semantic segmentation proposed by (Long et al., 2015) transforms the fully connected layers of CNNs into convolutional layers, enabling end-to-end mapping learning. This FCN method can be described as follows:

$$y = Net(x;\Theta) = S\left(K_2^* \left(M\left(R(K_1^* x + b_1)\right)\right) + b_1\right) \tag{3}$$

where $Net(x;\Theta)$ represents the FCN and the nonlinear mapping of the network, and x,y represent the input and output of the network, respectively. $\Theta = \{K_1, K_2, b_1, b_2\}$ is the set of parameters to be learned, including the convolution weights (K_1,K_2) and biases (b_1,b_2). $R(K_1^* x + b_1)$ represents a nonlinear activation function, such as the rectified linear unit (Dah et al., 2013) or the sigmoid or exponential linear units (Clevert et al., 2015). The ReLU activation function was employed in the model due to its advantage in mitigating the vanishing gradient problem. $M(\cdot)$ represents a subsampling function (e.g., max pooling or average pooling). * is the convolution operation, and $S(\cdot)$ represents the soft-max function.

$$\phi_1 = \| H_\Theta d_t - m_t \|^2 \tag{4}$$

In the Eq. (4), ϕ_1 is the loss function value, d_t are the input data of the training network, m_t are the output data of the training network, and H_Θ is a model parameter of the network.

$$m_p = H_\Theta d_{obs} \tag{5}$$

In the Eq. (5), d_{obs} is the noisy magnetotelluric data, and m_p is the predicted denoised magnetotelluric data.

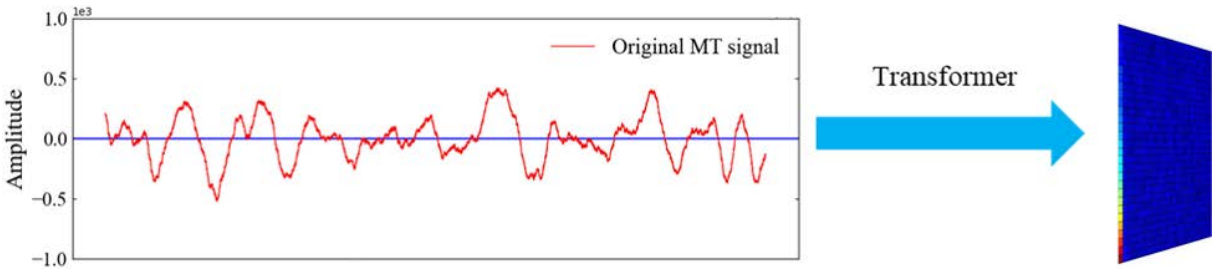

Figure 6. Signal-to-image Transformation.

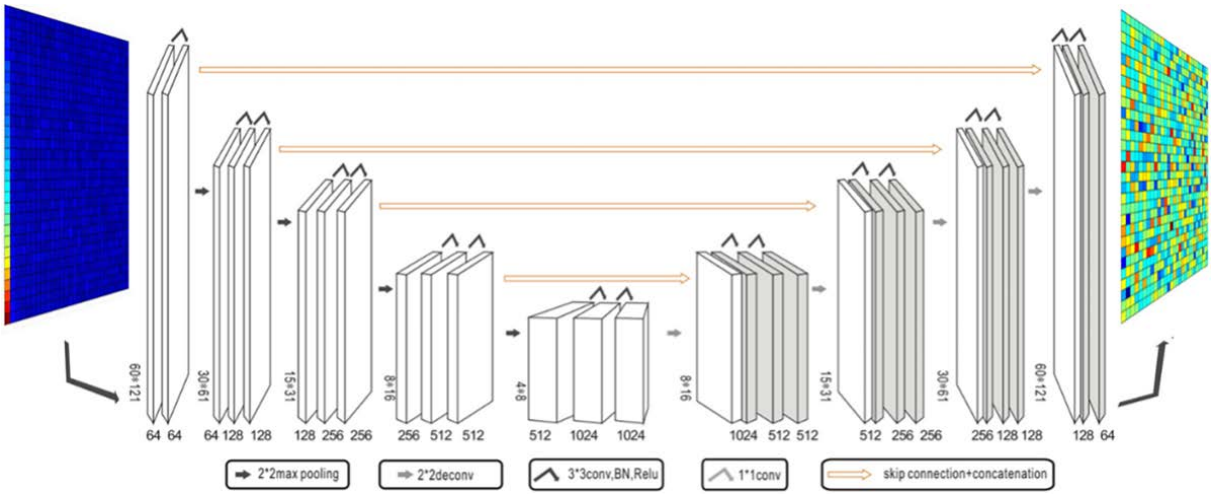

Figure 7. The architecture of the denoiser.

U-Net is a specific type of Fully Convolutional Networks (FCN). In order to improve feature extraction and increase sensitivity to subtle signal characteristics, we have adopted and modified the original U-Net architecture proposed by Ronneberger et al. (2015). The U-Net consists of a contracting path (encoder) on the left, which captures contextual and structural information, and a symmetric expanding path (decoder) on the right, which enables precise localisation. This symmetric encoder-decoder architecture uses a series of maximum pooling operations in the encoder and transposed convolutions in the decoder to progressively compress and reconstruct the input data.

In our implementation, we use a fixed 3×3 convolutional kernel. As the network depth increases, the effective receptive field expands, enabling the model to learn hierarchical features. Specifically, the number of feature channels in the encoder path increases in steps of 64, 128, 256, 512 and 1024. To preserve low- and high-level features, we use skip connections to merge shallow feature maps from the decoder with deeper feature maps from the encoder, facilitating learning of local and global structures (Fig. 7).

To adapt the U-Net architecture for denoising magnetotelluric (MT) signals, two key modifications are introduced. Firstly, unlike the original U-Net, which was designed for RGB image processing and has an input consisting of three colour channels, we adapt the network to handle MT data, which is represented as two-dimensional signal matrices. Secondly, in conventional U-Net applications, the output remains in the same domain as the input image. In contrast, our objective is to perform domain projection: the network maps noisy MT data to a denoised representation. To accomplish this, we ensure that the final 3×3 convolutional layer produces a feature map of the same size as the input, thereby directly transforming the raw MT signal into a cleaned, denoised version.

In deep learning, the workflow usually involves two main stages: training and prediction. To train the network effectively, a large dataset of paired "clean" and "noisy" MT signals was required. Since obtaining strictly noise-free field data is practically impossible, we generated a synthetic dataset consisting of 30,00 samples. The clean MT signals were simulated based on 1D magnetotelluric forward modeling over layered earth models. We randomly generated 3- to 5-layer geoelectric models with resistivities ranging from 10 Ω·m to 10,000 Ω·m and layer thicknesses varying from 100 m to 5,000 m. To simulate realistic field conditions, we added noise to these clean signals. The noise consisted of Gaussian white noise combined with random impulsive disturbances, with Signal-to-Noise Ratios (SNR) randomly distributed between 5 dB and 20 dB to ensure the network's robustness against varying noise levels. The training process aimed to minimize the Mean Squared Error (MSE) loss between the network output and the ground-truth clean signals. The network was trained using the Adam optimizer with an initial learning rate of 1×10^{-4}. The batch size was set to 64, and the training was conducted for 200 epochs. The dataset was split into a training set (80%) and a validation set (20%) to monitor convergence and prevent overfitting.

During the prediction stage, the trained network processes new, unseen noisy MT data. These inputs are fed into the model, which then produces the corresponding denoised MT data. This enables efficient, automated noise reduction in practical applications.

4. Results

The interpretation of the geophysical exploration data is carried out on the basis of indoor data processing using RES2DINV software for inversion profiling, with the RMS error controlled below 10%. This is combined with the actual situation of the site and geological data, and the geophysical exploration results are explained separately in the unit of measurement line.

4.1 ERT

4.1.1 HXWS-01 cross section of the tunnel inlet

The section of tunnel under investigation is located at the entrance and spans 1,510 m. It is oriented transversely relative to the tunnel axis, with a directional alignment of 121°. Surface investigations, including density measurements and route surveys, suggest that the area has dense vegetation and steep topography. The electrical resistivity tomography (ERT) cross-section shows significant variation in apparent resistivity, ranging from 80 Ω·m to 1,100 Ω·m. These resistivity values are consistent with audio geodetic sounding findings. According to Fig. 8, the surface cover layer of this section extends to a depth of between 0 m and 11 m. In the south-eastern portion, a 70 m segment intersecting the tunnel axis exhibits a lower resistivity, which is potentially linked to a valley zone. Furthermore, the low resistivity observed between lateral distances of 1,960 and 2,460 m suggests the presence of a highly weathered layer. Consequently, tunnel construction in this area requires particular attention to be paid to the challenges associated with water seepage and structural stability.

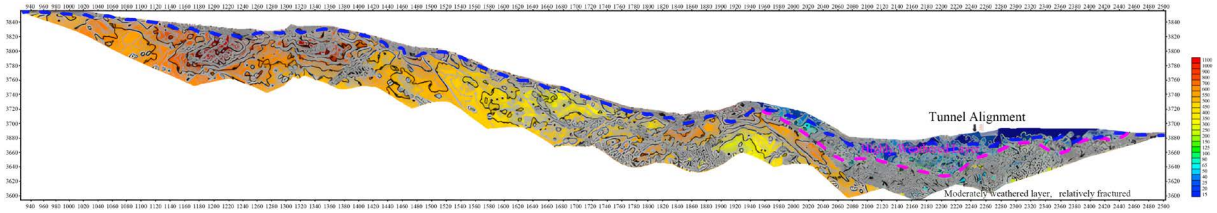

Figure 8. Resistivity model section obtained from ERT inversion for profile HXWS-01.

4.1.2 HXWS-02 cross section of the tunnel inlet

This section is located at the entrance of the tunnel, with section length 745 m, transverse cutting of the tunnel axis, and section direction 127°. According to the surface density work and route exploration, the surface vegetation of the profile is dense and the profile is relatively flat. The overall change of the resistivity is relatively stable, the resistivity change range is 150 Ω·m to 700 Ω·m, the resistivity value corresponds to the results of the buried depth of 1 m-8 m at the depth of the 90 m, at the distance of 440 m to 560 m, the depth of 20 m is assumed that the anomaly of different lithological contact zones, as shown in Fig. 9.

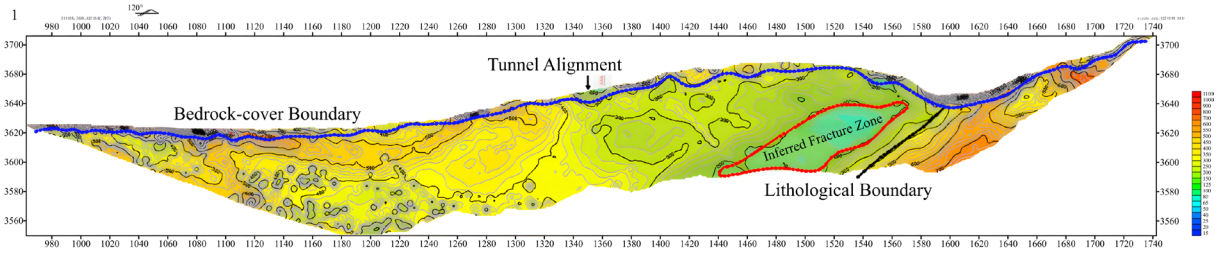

Figure 9. Resistivity model section obtained from ERT inversion for profile HXWS-02.

4.1.3 HXWS-03 cross section of the tunnel inlet

This section is located at the entrance of the tunnel, and the section length is 745 m, transverse to the tunnel axis, and the section direction is 133°. According to the surface ERT work and route exploration, the surface of the section is dense vegetation, the southeast section is steep, and approximately parallel to the HXWS-02 section. The overall change of ERT cross section is relatively stable, the resistivity range is 150 Ω·m to 900 Ω·m, and the resistivity value corresponds to the audio electromagnetic sounding results. If the surface cover is 1 m-12 m, the formation is stable within 80 m at the tunnel axis, in the distance of 500 m to 580 m, at depths of 40 m-50 m, the southeast abnormality is speculated as the stratum boundary, and the low resistance zone is not water fracture caused by different lithological contact zones, as shown in Fig. 10.

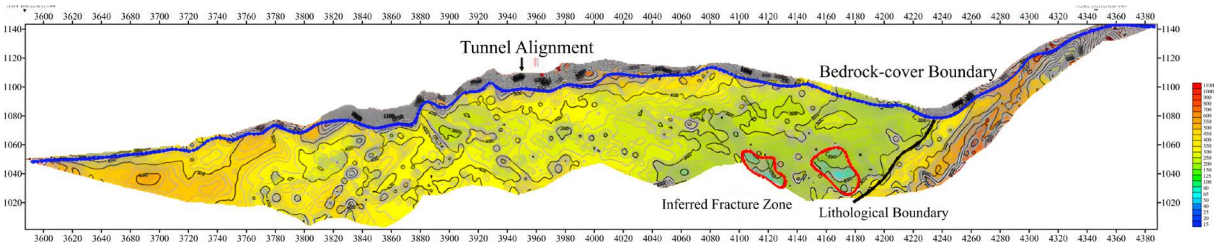

Figure 10. Resistivity model section obtained from ERT inversion for profile HXWS-03.

4.1.4 Main section of ZXWS-03 at the tunnel outlet

This section is located at the entrance of the tunnel, approximately parallel to the tunnel axis, and the section is 238°. This section is 545 m long. According to the surface ERT work and route exploration, the surface vegetation of the section is dense, and the overall cutting of the section is large. The overall change of apparent resistivity of ERT cross section is relatively stable, and the resistivity change range is 250 Ω·m to 900 Ω·m. The resistivity value corresponds to the audio electromagnetic sounding results. From the drawing, the surface cover layer of this section is 1 m-10 m, abnormal, and the resistivity increases at about 450 m, which is estimated as the lithologic boundary, as shown in Fig. 11.

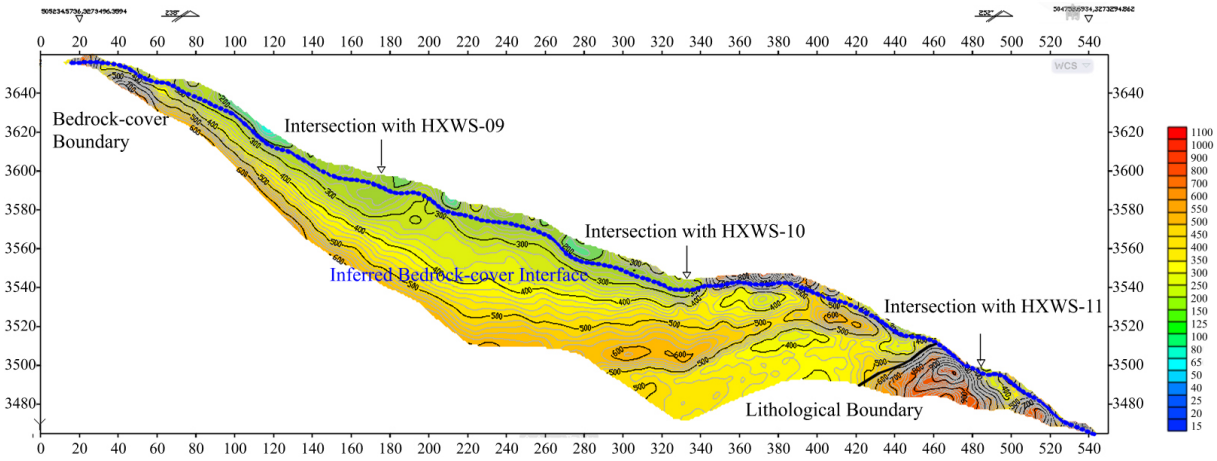

Figure 11. Resistivity model section obtained from ERT inversion for profile HXWS-09.

4.1.5 HXWS-09 cross section of the tunnel outlet

This section is located at the entrance of the tunnel, crossing the main section of ZXWS-03, and the section direction is 334°. This section is 295 m long. According to the surface ERT work and route exploration, the surface vegetation of this section is dense and relatively flat. The overall change of apparent resistivity of ERT cross section is relatively stable, and the resistivity change range is 250 Ω·m to 800 Ω·m. The resistivity value corresponds to the AMT sounding results. From the figure, the surface cover layer of this section is 1 m-7 m deep, with no anomalies of aquifer and broken zone, as shown in Fig. 12.

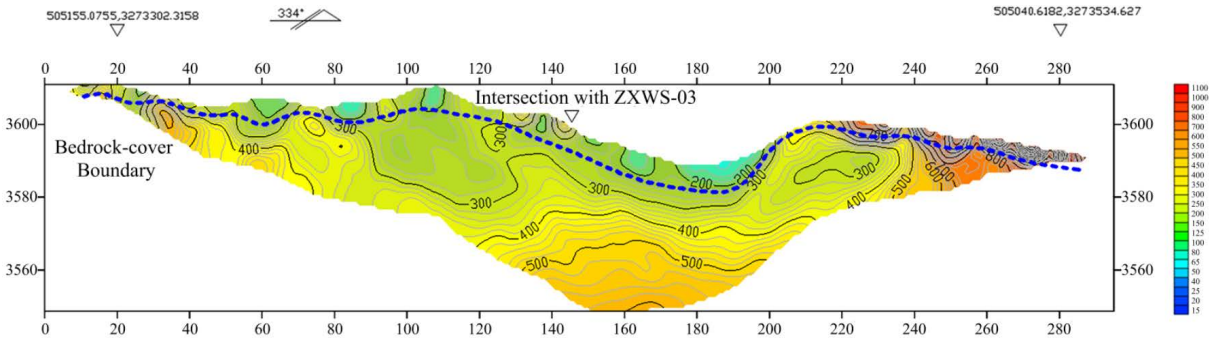

Figure 12. Resistivity model section obtained from ERT inversion for profile HXWS-09.

4.1.6 HXWS-10 cross section of the tunnel exit

This section is located at the entrance of the tunnel, crossing the main section of ZXWS-03, and the section direction is 342°. This section is 195 m long. According to the surface density work and route exploration, the surface vegetation of this section is dense and the surface is undulating. The overall change of apparent resistivity of ERT cross section is relatively stable, and the resistivity change range is 150 Ω·m to 800 Ω·m, and the resistivity value corresponds to the AMT sounding results. From the figure, the surface cover of this section is 1 m-5 m, with no anomalies of aquifer and broken zone, as shown in Fig. 13.

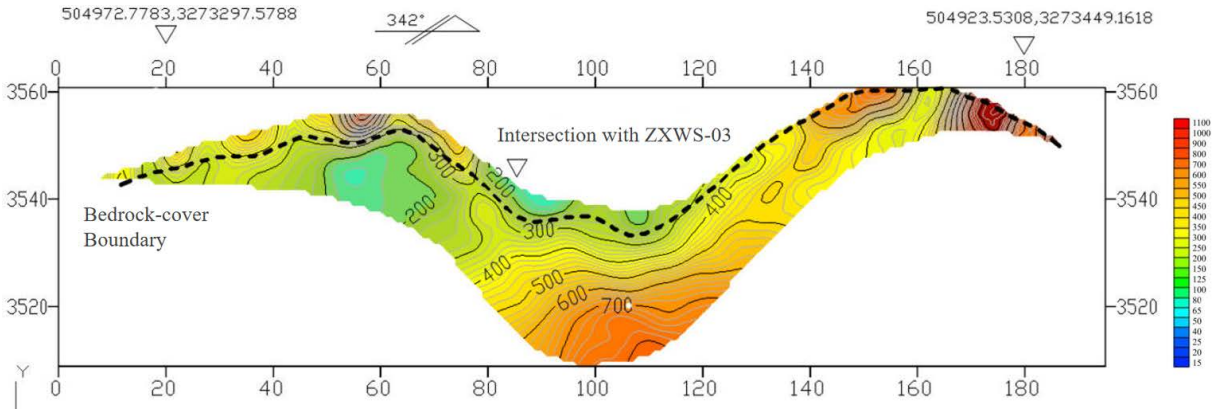

Figure 13. Resistivity model section obtained from ERT inversion for profile HXWS-10.

4.1.7 HXWS-11 cross section of the tunnel outlet

This section is located at the entrance of the tunnel, crossing the main section of ZXWS-03, and the section direction is 353°. This section lenth is 195 m. According to the surface ERT work and route exploration, the surface vegetation of this section is dense and the terrain is relatively gentle. The overall change of apparent resistivity of ERT cross section is relatively stable, and the resistivity change range is 300 Ω·m to 800 Ω·m. The resistivity value corresponds to the AMT sounding results. From the figure, the buried depth of this section is 0.5 m-5 m, with no anomalies in aquifer and broken zone, as shown in Fig. 14.

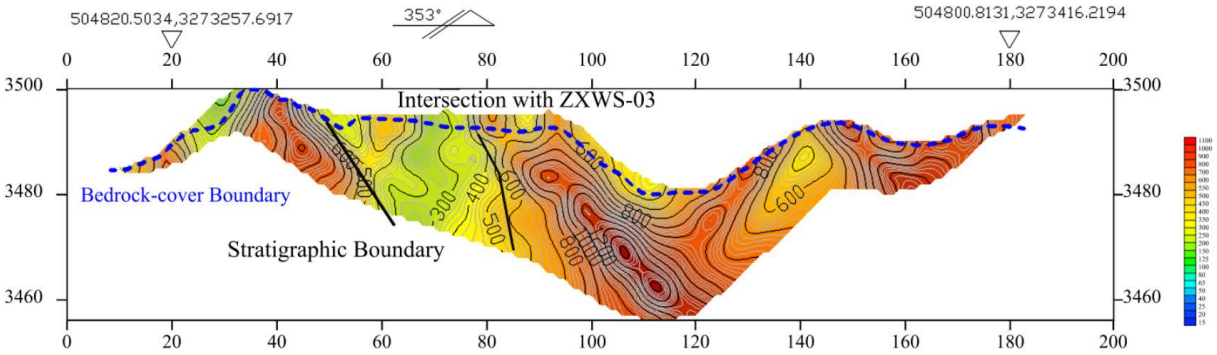

Figure 14. Resistivity model section obtained from ERT inversion for profile HXWS-11.

4.2 AMT sounding (EM3D)

4.2.1 Main line of the tunnel (K10 + 570~K19 + 210)

Near the tunnel axis, the range of apparent resistivity variations is relatively stable, indicating a strong correlation with changes in the rock type. Based on the two-dimensional resistivity inversion profile, the rock mass at the depth of the tunnel exploration can be divided into five lithological sections. Geological mapping reveals gneiss, biotite granodiorite, quartz diorite and biotite gneiss to be present. Due to intrinsic resistivity differences, biotite gneiss exhibits noticeable fluctuations and, overall, has lower resistivity than 'pure' gneiss. Of all the lithologies encountered, diorite has the highest resistivity, while biotite granodiorite shows slightly lower (but still elevated) resistivity values (Fig. 15).

In the 0-2000 m lateral portion, two distinct resistivity anomalies are interpreted as fractured zones resulting from tectonic activity or natural jointing. Inversion results indicate that these fractured zones are essentially dry, as there are no significant low-resistivity signatures typically associated with groundwater. This lack of saturation implies that the integrity of the rock mass in these areas is compromised. Furthermore, resistivity patterns suggest that this portion of the profile has been substantially influenced by past magmatic intrusions, leading to localised heterogeneities in electrical properties.

In the lateral 3000-5600 m portion, a pronounced high-resistivity body appears, which can be attributed to quartz-rich (quartzose) lithology. The resistivity map shows that the corresponding rock mass is well-connected and structurally sound, with no evidence of water-bearing or intensely fractured zones. Consequently, this sector is interpreted as a relatively coherent block of hard, quartz-dominated rock.

In the 5600-9300 m lateral portion, resistivity values remain fairly uniform and there are no obvious anomalies indicating major fracture zones or saturated bodies. Compared to the preceding segment, the lithological characteristics appear to have changed, as evidenced by the lack of pronounced resistivity contrasts. Rather than structural discontinuities or fluid saturation, the subtle variations observed in the resistivity map likely reflect different degrees of metamorphic alteration within a predominantly homogeneous rock unit.

The AMT resistivity inversion section, combined with structural interpretation, provides a comprehensive insight into the lithological and tectonic controls along the main tunnel alignment. Overall, apparent resistivity near the tunnel axis shows smooth and continuous variations, indicating a strong correlation with changes in rock type

rather than the influence of groundwater. The two-dimensional inversion profile enables the rock mass at tunnel depth to be subdivided into five distinct lithological sections, which is in good agreement with geological mapping results identifying gneiss, biotite gneiss, biotite granodiorite, and quartz diorite. Hence, the AMT data confirm that the tunnel alignment is largely conducive to construction, with stable rock masses prevailing in the outlet and mid-to-late main line sections. However, critical inlet areas and early fractured zones require enhanced engineering precautions to address weathering, potential seepage and integrity concerns.

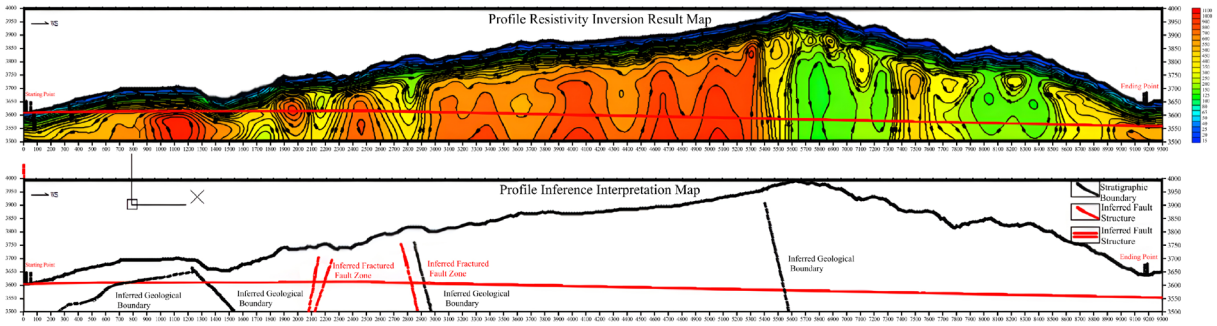

Figure 15. Resistivity model section obtained from AMT inversion along the main tunnel alignment and the corresponding structural interpretation.

4.2.2 Parallel profile of the main line ZXWS-02

This section is located at the exit of the tunnel and arranged along the direction of the main survey line. From the section inversion results, there is no anomaly such as crushing zone and aquifer, the resistivity range is 300 Ω·m-800 Ω·m, the rock mass is stable, and the resistivity has certain fluctuation due to the change of lithology or metamorphic degree, as shown in Fig. 16.

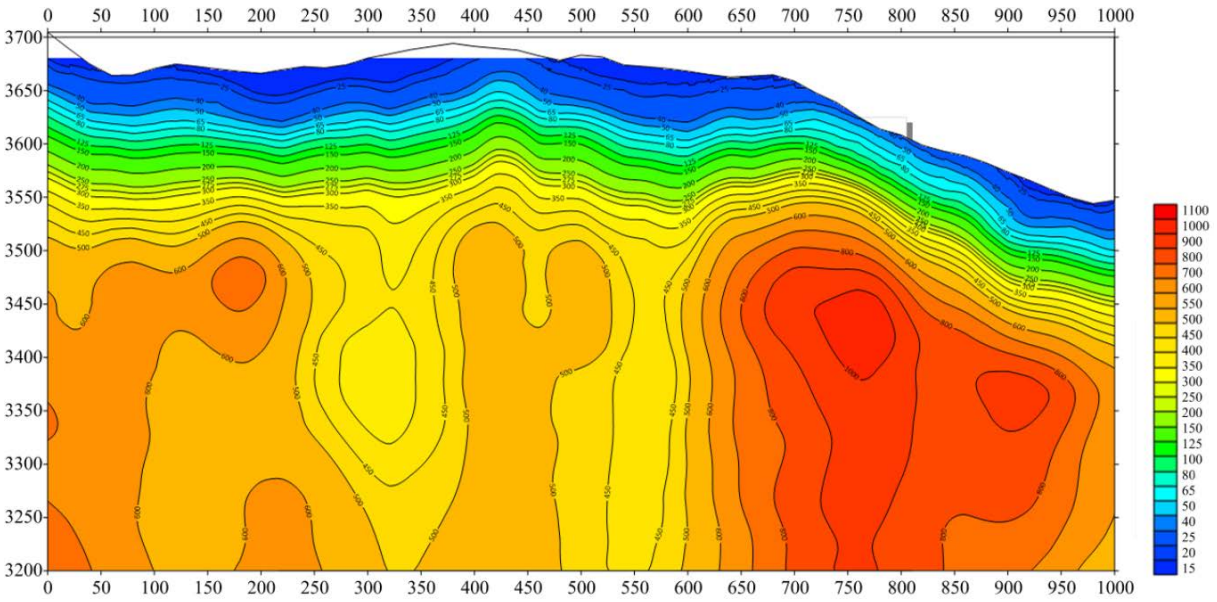

Figure 16. Resistivity model section obtained from AMT inversion for profile ZXWS-02.

4.2.3 Cross-cut section HXWS-04

This section is located at the entrance of the tunnel, and the main measuring line is arranged horizontally. According to the section inversion results, there is no anomalies such as crushing zone and aquifer on the whole, the resistivity range is 300 Ω·m-800 Ω·m, and the overall rock mass is stable, as shown in Fig. 17.

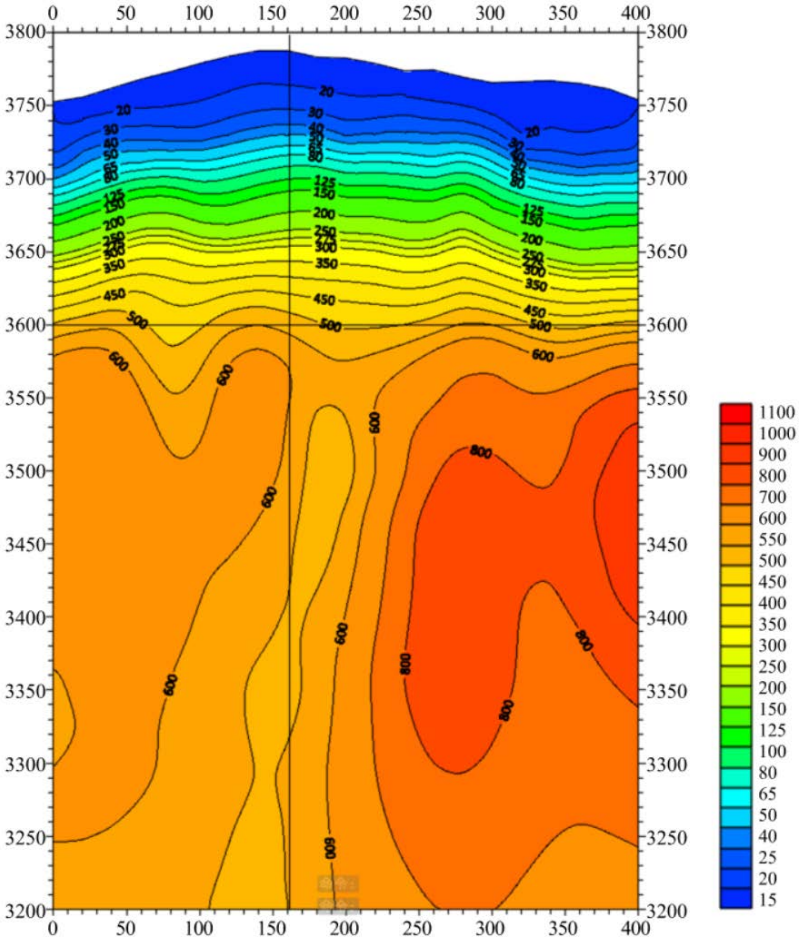

Figure 17. Resistivity model section obtained from AMT inversion for profile HXWS-04.

4.2.4 Cross-cut section HXWS-05

This section is located at the entrance of the tunnel, and the main survey line is arranged horizontally. According to the section inversion results, there is no anomalies such as fracture zone and aquifer, the resistivity range is 300 Ω·m-1000 Ω·m, the rock mass is relatively stable, lithologic changes or different deterioration, and the resistivity has certain fluctuations, as shown in Fig. 18.

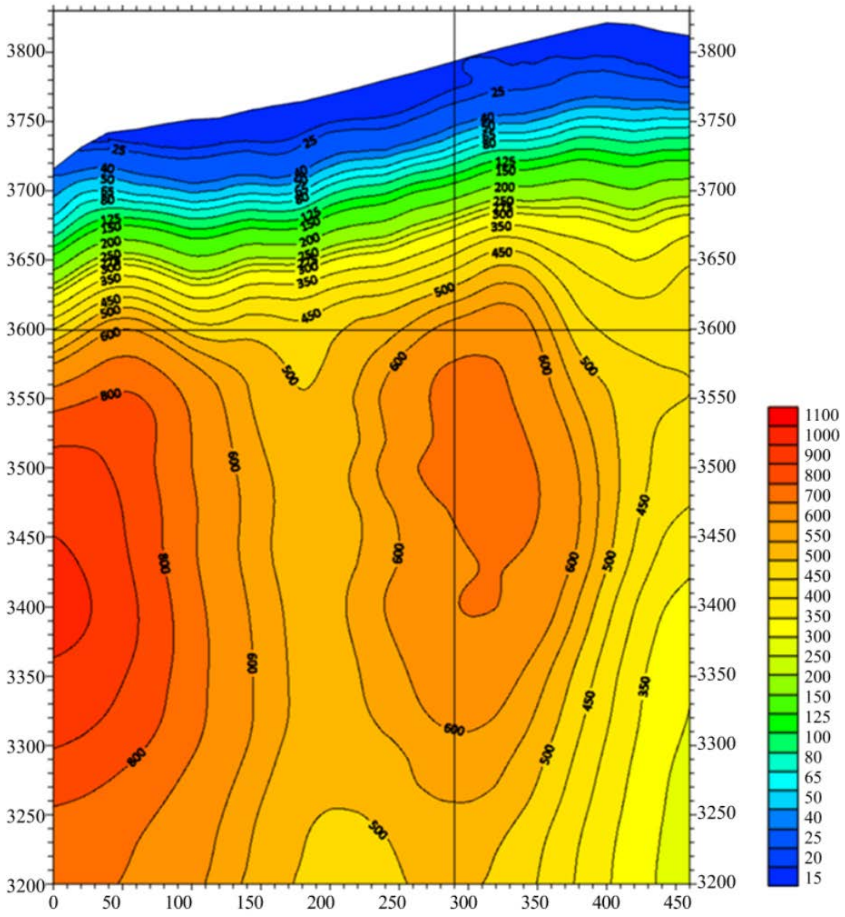

Figure 18. Resistivity model section obtained from AMT inversion for profile HXWS-05.

4.2.5 Cross-cut section HXWS-06

This section is located at the entrance of the tunnel, and the main survey line is arranged horizontally. According to the section inversion results, the deep lithology changes greatly, so it is inferred that there is a fracture or fracture zone with no water content, and the tunnel axis position is stable, and there is no significant lithology change, as shown in Fig. 19.

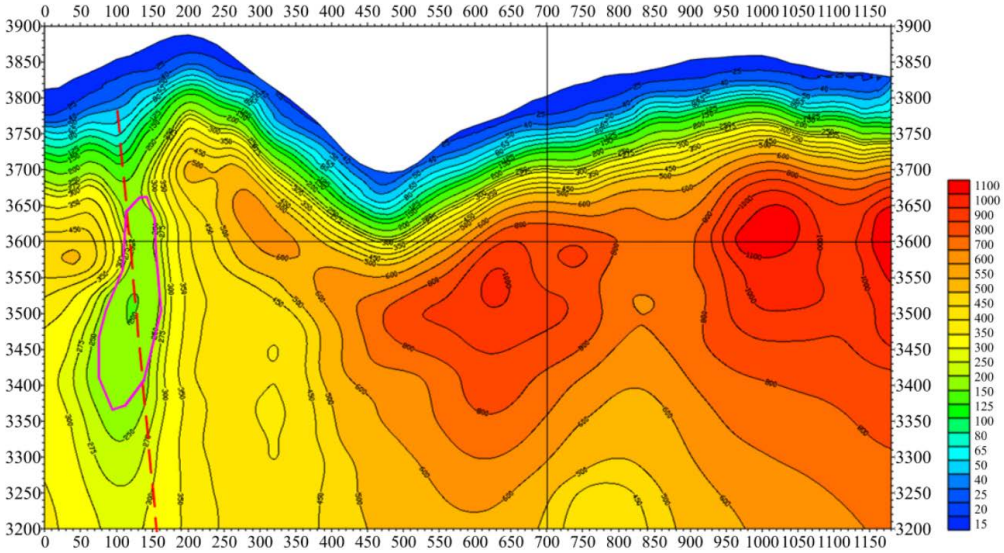

Figure 19. Resistivity model section obtained from AMT inversion for profile HXWS-06.

4.2.6 Cross-cut section HXWS-07

This section is located at the entrance of the tunnel, and the main survey line is arranged horizontally. According to the section inversion results, the deep lithology changes greatly, so it is inferred that there is a fracture or fracture zone with no water content. The resistivity of this section is low compared with the previous sections, as shown in Fig. 20.

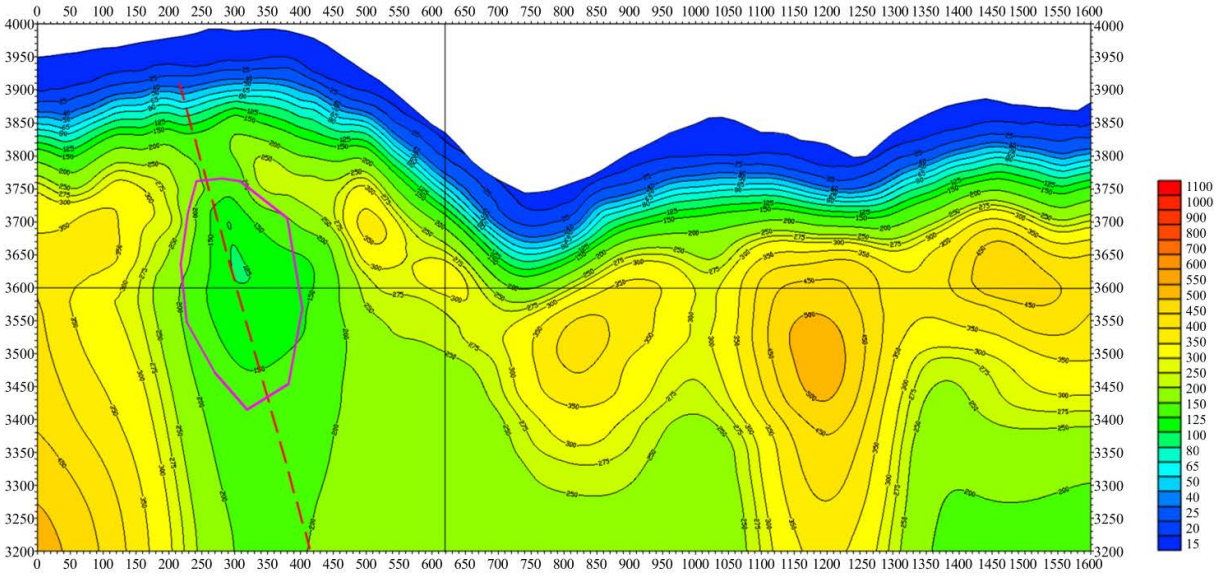

Figure 20. Resistivity model section obtained from AMT inversion for profile HXWS-07.

4.2.7 Cross-cut section HXWS-08

This section is located at the entrance of the tunnel, and the main measuring line is arranged horizontally. According to the section inversion results, there is no anomaly such as crushing zone and aquifer, the resistivity range is 500 Ω·m-1000 Ω·m, and the overall rock mass is stable, as shown in Fig. 21.

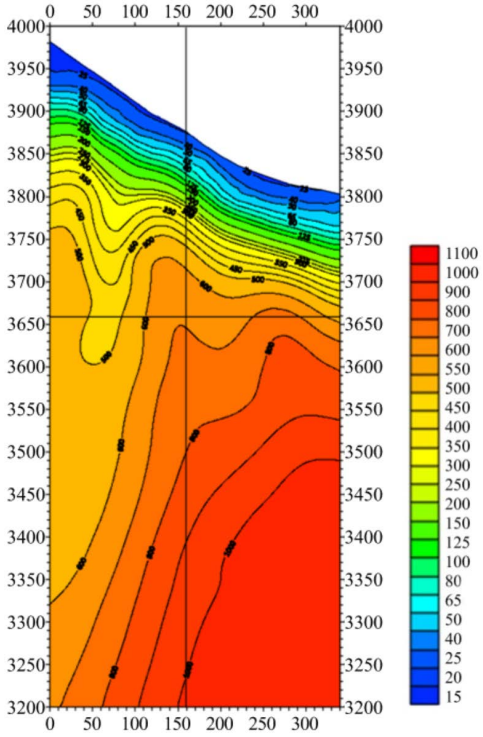

Figure 21. Resistivity model section obtained from AMT inversion for profile HXWS-08.

5. Discussion and Conclusions

Electrical Resistivity Tomography (ERT) and U-Net deep learning-denose Audio-Magnetotelluric (AMT) can effectively determine the location, width, and occurrence of low-resistivity structures in the near-surface Quaternary unconsolidated accumulative layers, revealing a detailed subsurface geological framework for the tunnel alignment. Comprehensive geophysical interpretation defines a bipartite engineering environment, delineating clear boundaries between stable bedrock sections and geologically complex zones. The majority of the route – specifically the central segments of the main line and the tunnel outlet – is structurally sound. In these sections, consistent high-resistivity signatures correlate with coherent metamorphic and igneous lithologies, such as quartz diorite and biotite granodiorite. These geophysical responses suggest favorable tunneling conditions with minimal evidence of significant aquifers or active tectonic instability.

The ERT-AMT integration complements investigation depth and shallow lateral resolution while enabling cross-validation, enhancing understanding of the study area and supporting tunnel excavation risk prediction. Geophysical data highlight key challenges concentrated at the tunnel inlet and the initial segments of the main line. ERT identifies significant resistivity variability and low-resistivity anomalies in the inlet area, indicative of highly weathered layers extending up to 11 m in depth. This weathering is likely exacerbated by valley intersections that facilitate groundwater accumulation and seepage. Furthermore, deep AMT data reveal dry fractured zones in the early segments of the main line. Although these zones currently lack fluid saturation, they interrupt rock competency and pose potential risks for roof stability and deformation during excavation.

Notably, these methods have limitations. ERT offers higher resolution for geological structures shallower than 50 m underground, and is an efficient geophysical method for detecting subsurface structures within this depth

range, while AMT achieves a greater detection depth but exhibits lower resolution for interlayer media in the subsurface. Since ERT and AMT rely on indirect measurements of apparent resistivity, the solutions are subject to non-uniqueness; for instance, low-resistivity zones may result from clay-rich sediments or conductive minerals rather than groundwater saturation. Therefore, while the geophysical model provides a robust baseline, it represents a prediction requiring validation.

Future efforts could integrate higher-resolution methods such as Tunnel Seismic Prediction (TSP), drilling data, and Ground Penetrating Radar (GPR) to overcome the limitations of individual techniques, especially in improving detection accuracy for deeply buried sections and structurally complex zones. It is also recommended to incorporate additional geological data for model calibration and updating, particularly for verifying initial resistivity anomalies. By increasing the number of borehole sampling points and conducting fracture density tests, more reliable baseline data can be provided for tunnel risk assessment.

Acknowledgements. We acknowledge the research was funded by University Natural Science Research Project of Anhui Province (Grant number 2022AH052475) and Quality Engineering Projects of Anhui Province (Grant number 2022SX115).

References

Araya-Polo, M., J. Jennings, A. Adler and T. Dahlke (2018). Deeplearning tomography. The Leading Edge, 37, 1, 58-66.

Aleardi, M., A. Vinciguerra, E. Stucchi, A. Hojat (2022). Probabilistic inversions of electrical resistivity tomography data with a machine learning-based forward operator, Geophys. Prospect., 70, 5, 938-957.

Aharon, M., M. Elad and A. Bruckstein (2006). K-SVD: An algorithm for designing overcomplete dictionaries for sparse representation, IEEE Trans, Signal Process., 54, 11, 4311-4322, doi:10.1109/TSP.2006.881199.

am Ende, B. A. (2012). Geophysics of Locating Karst and Caves. Encyclopedia of Caves (Second Edition), 348-352, doi:10.1016/B978-0-12-383832-2.00048-7.

Cai, J. and Q. Chen (2015). Spectrum analysis of magnetotelluric data series based on EMD-teager transform, Pure Appl. Geophys., 172, 2901-2915, doi:10.1007/s00024-015-1083-0.

Chen, H., R. Guo, J. Liu et al. (2020). Magnetotelluric data denoising with recurrent neural network. In SEG 2019 Workshop: Mathematical Geophysics: Traditional vs Learning, Beijing, China, 5-7 November 2019,116-118, Society of Exploration Geophysicists, doi:10.1190/iwmg2019_28.1.

Clevert, D., T. Unterthiner and S. Hochreiter (2015). Fast and accurate deep network learning by exponential linear units (elus), arXiv preprint arXiv:1511.07289.

Dahl, G. E., T. N. Sainath and G. E. Hinton (2013). Improving deep neural networks for LVCSR using rectified linear units and dropout. In 2013 IEEE international conference on acoustics, speech and signal processing, 8609-8613, doi:10.1109/ICASSP.2013.6639346.

Durdağ, D., M. Göktuğ Drahor and M. Sadık Yağlıdere (2023). Combined application of electrical resistivity tomography and multi-channel analysis of surface waves methods in the tunnel detection: A case study from Kocaeli University Campus Site, Turkey, J. Appl. Geophys., 208, 104895, doi:10.1016/j.jappgeo.2022.104895.

De Benedetto, D., A. Castrignano, D. Sollitto et al. (2012). Integrating geophysical and geostatistical techniques to map the spatial variation of clay, Geoderma, 171, 53-63, doi:10.1016/j.geoderma.2011.05.005.

Deshmukh, V., P. V. Vijaya Kumar, P. B. V. Subba Rao et al. (2022). Audiomagnetotelluric (AMT) studies across Aravali-Tural-Rajawadi geothermal zones, western Maharastra, India, J. Appl. Geophys., 1, 98, 104579, doi:10.1016/j.jappgeo.2022.104579.

Festi, P., G. Bossi, M. Francioni et al. (2023). Structural health of a road tunnel intersecting a large and active rock-block slide, Italian J. Engin. Geol. Environ., 49-55, doi:10.4408/IJEGE.2023-01.S-07.

Fäth. J. and C. Kneisel (2024). Combined 2D- and 3D ERT monitoring as a geophysical tool for investigating spatial and temporal soil moisture fluctuations in a pine-beech forest, Trees, Forests and People, 16, 100555, doi:10.1016/j.tfp.2024.100555.

Fichtner, A., A. Zunino and L. Gebraad (2019). Hamiltonian Monte Carlo solution of tomographic inverse problems, Geophys. J. Int., 216, 2, 1344-1363, doi:10.1093/gji/ggy496.

Fuji-ta, K., Y. Ogawa, M. Ichiki et al. (1999). Audio frequency magneto-telluric survey of Norikura Volcano in central Japan, J. Volcanol. Geotherm. Res., 90, 209-217, doi:10.1016/S0377-0273(99)00020-7.

Garcia, X. and A. G. Jones (2008). Robust processing of magnetotelluric data in the AMT dead band using the continuous wavelet transform, Geophys., 73, 6, F223-F234, doi:10.1190/1.2987375.

Genetu, M. and G. Mewa (2023). Integrated geophysics for investigation of landslide-affected site located near to Alemketema town, Central Ethiopia, J. Appl. Geophys., 216, 105162, doi:10.1016/j.jappgeo.2023.105162.

Ghalati, F. H., J. A. Craven, D. Motazedian et al. (2022). Modeling a fractured geothermal reservoir using 3-D AMT data inversion: Insights from Garibaldi Volcanic Belt, British Columbia, Canada, Geothermics,105, 102528, doi:10.1016/j.geothermics.2022.102528.

Gomo, M. (2023). Use of electric potential difference in audio magnetotelluric (AMT) geophysics for groundwater exploration, Groundwater for Sustainable Development, 20, 100864, doi:10.1016/j.gsd.2022.100864.

Guo Z., X. Gong, J. Han et al. (2022). Research on a multiscale denoising method for low signal-to-noise magnetotelluric signal, IEEE Trans. Geosci. Remote Sensing, 60, 1-18, doi:10.1109/TGRS.2022.3229160.

Hu, J., J. Zhou, H. Tan, Z. Ni, Z. Zhu et al. (2025). Geologic Characteristics and Age of Beryllium Mineralization in the Jiulong Area, the Southeast Edge of the Western Kunlun-Songpan-Ganzi Rare Metal Metallogenic Belt, Minerals, 15, 3, 253, doi:10.3390/min15030253.

Imani, P., G. Tian, S. Hadiloo and A. Abd El-Raouf (2021). Application of combined electrical resistivity tomography (ERT) and seismic refraction tomography (SRT) methods to investigate Xiaoshan District landslide site: Hangzhou, China, J. Appl. Geophys., 184, 104236, doi:10.1016/j.jappgeo.2020.104236.

Lanfang, H., M. H. Feng, H. Zhanxiang and X. B. Wang (2006). Application of EM Methods for the Investigation of Qiyueshan Tunnel, China, J. Environ. Engin. Geophys., 11, 151-156, doi:10.2113/JEEG11.2.151.

LeCun, Y., Y. Bengio and G. Hinton (2015). Deep learning, Nature, 521, 7553, 436 444, doi:10.1038/nature14539.

Li, G., X. Liu, J. Tang et al. (2020). Improved shift-invariant sparse coding for noise attenuation of magnetotelluric data, Earth Planets Space, 72, 45, doi:10.1186/s40623-020-01173-7.

Li, G., X. Liu, J. Tang. et al. (2020). Denoising low-frequency magnetotelluric data using mathematical morphology filtering and sparse representation, J. Appl. Geophys., 172, 103919, doi:10.1016/j.jappgeo.2019.103919.

Li, J., Y. Peng, J. Tang et al. (2021). Denoising of magnetotelluric data using K-SVD dictionary training, Geophys. Prospect., 69, 2, 448-473, doi:10.1111/1365-2478.13058.

Li, J., F. Ma, J. Tang et al. (2022). Denoising application of magnetotelluric low-frequency signal processing, IEEE Trans. on Geosci. Remote Sens., 60, 1-18, doi:10.1109/TGRS.2022.3210334.

Li, Y., M. Zhang, Y. Zhao et al. (2022). Distributed acoustic sensing vertical seismic profile data denoising based on multistage denoising network, IEEE Trans. Geosci. Remote Sens., 60, 1-17, doi:10.1109/TGRS.2022.3194635.

Li, G., X. Gu, Z. Ren et al. (2022). Deep learning optimized dictionary learning and its application in eliminating strong magnetotelluric noise, Minerals, 12, 8, doi:10.3390/min12081012.

Li, J., Y. Luo, G. Li et al. (2024). Atom-profile updating dictionary learning with nucleus sampling attention mechanism sparse coding for audio magnetotelluric denoising, Geophysics, 89, 3, E73-E85, doi:10.1190/geo2023-0205.1.

Long, J., E. Shelhamer and T. Darrell (2015). Fully convolutional networks for semantic segmentation, In Proceedings of the IEEE conference on computer vision and pattern recognition, 3431-3440.

Medsker, L. R. and L. Jain (2001). Recurrent neural networks, Design and Applications, 5, 64-67, 2.

Moreira, C. A., V. Rosolen, L. Moreira Furlan et al. (2021). Hydraulic conductivity and geophysics (ERT) to assess the aquifer recharge capacity of an inland wetland in the Brazilian Savanna, Environ. Challenges, 5, 100274, doi:10.1016/j.envc.2021.100274.

Nabighian, M. and J. Macnae (1991). The magnetotelluric method[J]. Electromagnetic methods in applied geophysics, 2, 427-520.

Neyshabur, B., S. Bhojanapalli, D. McAllester and N. Srebro (2017). Exploring generalization in deep learning, Adv. Neural Info. Proc. Sys., 30, 1-10.

O'Shea, K. (2015). An introduction to convolutional neural networks. arXiv preprint arXiv:1511.08458.

Park, S., T. Panagiotis and S. Shin (2022). Electrical resistivity tomography (ERT) monitoring of leachate seepage from an animal carcass waste (ACW) facility, South Korea, J. Appl. Geophys., 206, 104809, doi:10.1016/j.jappgeo.2022.104809.

Rathnayaka, S., C. D. Gustafson, D. Yoxtheimer et al. (2024). Imaging freshwater and saline aquifers beneath Bradford County, Pennsylvania, USA, using Audio-Magnetotelluric (AMT) data, J. Appl. Geophys., 220, 105255, doi:10.1016/j.jappgeo.2023.105255.

Ren, W., Z. Ren, G. Xue et al. (2023). Three-dimensional audio magnetotelluric imaging of the Yangyi geothermal field in Tibet, China, J. Appl. Geophys., 211, 104966, doi:10.1016/j.jappgeo.2023.104966.

Ronneberger, O., P. Fischer and T. Brox (2015). U-net: Convolutional networks for biomedical image segmentation. In Medical image computing and computer-assisted intervention – MICCAI 2015: 18th international conference, part III 18, 234-241, doi:10.1007/978-3-319-24574-4_28.

Russolillo, A., F. Foresta Martin, A. Merico et al. (2024). Unveiling a hidden fortification system at "Faraglioni" Middle Bronze Age Village of Ustica Island (Palermo, Italy) through ERT and GPR prospections, J. Appl. Geophys., 220, 105272, doi:10.1016/j.jappgeo.2023.105272.

Tang, J. T., L. Guang, C. Zhou et al. (2018). Denoising AMT data based on dictionary learning, Chinese Journal of Geophysics (in Chinese), 61, 9, 3835-3850, doi:10.6038/cjg2018L0376.

Trad, D. O. and J. M. Travassos (2000). Wavelet filtering of magnetotelluric data, Geophysics, 65, 2, 482-491, doi:10.1190/1.1444742.

Verdet, C., C. Sirieix, A. Marache, J. Riss et al. (2020). Detection of undercover karst features by geophysics (ERT) Lascaux cave hill, Geomor., 360, 107177, doi:10.1016/j.geomorph.2020.107177.

Wang, T.-P., C.-C. Chen, L.-T. Tong et al. (2015). Applying FDEM, ERT and GPR at a site with soil contamination: A case study, J. Appl. Geophys., 121, 21-30, doi:10.1016/j.jappgeo.2015.07.005.

Wang, G., D. Lei, Z. Zhang et al. (2018). Tensor CSAMT and AMT Studies of the Xiarihamu Ni-Cu Sulfide Deposit in Qinghai, China, J. Appl. Geophys.,159,795-802, doi:10.1016/j.jappgeo.2018.09.031.

Wang, Q,, H. Li, S. Xia et al. (2022). Geometry of the Quaternary strata along the middle segment of the Longmen Shan and its formation mechanism: Insights from AMT, ERT and borehole data, Tectonophysics, 826, 229226, doi:10.1016/j.tecto.2022.229226.

Wang, N., S. Zhao, J. Hui et al. (2017). Three-dimensional audio-magnetotelluric sounding in monitoring coalbed methane reservoirs, J. Appl. Geophys., 138, 198-209, doi:10.1016/j.jappgeo.2017.01.028.

Wu, Z. and N. E. Huang (2009). Ensemble empirical mode decomposition: a noise-assisted data analysis method, Adv. Adapt. Data An., 1, 01, 1-41, doi:10.1142/S1793536909000047.

Ren, W., Z. Ren, G. Xue et al. (2023). Three-dimensional audio magnetotelluric imaging of the Yangyi geothermal field in Tibet, China, J. Appl. Geophys., 211, 104966, doi:10.1016/j.jappgeo.2023.104966.

Yang, S., H. Tan, Z. Li, J. Hu et al. (2024). Metallogenic chronology and prospecting indication of Tiechanghe granite and polymetallic molybdenum mineralization types in Jiulong area, western Sichuan, China, Minerals, 14, 9, 909, doi:10.3390/min14090909.

Zhenwei, G., X. G. Xue, J. Liu and X. Wu (2020). Electromagnetic methods for mineral exploration in China: A review, Ore Geology Reviews, 118, 103357, doi:10.1016/j.oregeorev.2020.103357.

Zhao, H, Q. Zhang, J. Tan et al. (2021). Research and application of AMT in tunnel hidden goaf under complex conditions, IOP Conference Series: Earth and Environmental Science, ISRM-ARMS11, doi:10.1088/1755-1315/861/5/052085.

Zhang, L., J. Tang, G. Li et al. (2022). Audio magnetotelluric denoising via variational mode decomposition and adaptive dictionary learning, J. Appl. Geophys., 204, 104748, doi:10.1016/j.jappgeo.2022.104748.

Zhang, X., L. Jiang, W. Deng, Z. Shu et al. (2024). Risk assessment of geological hazards in the Alpine Gorge region and its influencing factors: A case study of Jiulong County, China, Sustainability, 16, 5, 1949, doi:10.3390/su16051949.

Zhu, T., J. Zhou, H. Wang (2017). Localization and characterization of the Zhangdian-Renhe fault zone in Zibo city, Shandong province, China, using electrical resistivity tomography (ERT), Journal of Applied Geophysics, 136, 343-352, doi:10.1016/j.jappgeo.2016.11.016.

***CORRESPONDING AUTHOR: Shuang LIANG**,
Civil Engineering Department, City University of Hefei, Hefei, Anhui, China
e-mail: p120121@siswa.ukm.edu.my